

Slitless Spectroscopy of LMC Planetary Nebulae. A Study of the Emission Lines and Morphology.¹

Letizia Stanghellini²

Space Telescope Science Institute, 3700 San Martin Drive, Baltimore, Maryland 21218,
USA; lstanghe@stsci.edu

Richard A. Shaw

National Optical Astronomy Observatory, 950 N. Cherry Av., Tucson, AZ 85719, USA;
shaw@noao.edu

Max Mutchler

Space Telescope Science Institute, 3700 San Martin Drive, Baltimore, Maryland 21218,
USA; mutchler@stsci.edu

Stacy Palen, Bruce Balick

Astronomy Department, Box 351580, University of Washington, Seattle WA 98195-1580;
palen@astro.washington.edu, balick@astro.washington.edu

and

J. Chris Blades

Space Telescope Science Institute; blades@stsci.edu

Received _____; accepted _____

²Affiliated with the Astrophysics Division, Space Science Department of ESA; on leave from INAF-Osservatorio Astronomico di Bologna

ABSTRACT

HST STIS slitless spectroscopy of LMC PN is the ideal tool to study their morphology and their ionization structures at once. We present the results from a group of 29 PN that have been spatially resolved, for the first time, in all the major optical lines. Images in the light of $H\alpha$, $[\text{NII}]$, and $[\text{OIII}]$ are presented, together with line intensities, measured from the extracted 1D and 2D spectra. A study on the surface brightness in the different optical lines, the electron densities, the ionized masses, the excitation classes, and the extinction follows, illustrating an ideal consistence with the previous results found by us on LMC PN. In particular, we find the surface brightness decline with the photometric radius to be the same in most emission lines. We find that asymmetric PN form a well defined cooling sequence in the excitation – surface brightness plane, confirming their different origin, and larger progenitor mass.

Subject headings: Stars: AGB and post-AGB — stars: evolution — planetary nebulae: general — Magellanic Clouds

1. Introduction

Planetary Nebulae (PNs) have been used extensively to gain insight into the late stages of evolution of low and intermediate mass stars. In particular, the observed nebular morphology reflects the geometry of the initial mass ejection during and shortly after the

¹Based on observations made with the NASA/ESA Hubble Space Telescope, obtained at the Space Telescope Science Institute, which is operated by the Association of Universities for Research in Astronomy, Inc., under NASA contract NAS 5–26555

AGB phase of stellar evolution followed by the cumulative dynamical effects of winds, heating by ultraviolet photons, plus the sudden increase in pressure from the passage of an ionization front. It is now widely accepted that PNs are the ejecta of ~ 1 to $8 M_{\odot}$ progenitor stars, expelled at the end of the thermally pulsating, Mira-like phase on the AGB. These ejecta travel at a low velocity, and remove most of the stellar envelope eventually exposing a white dwarf core.

Most PNs show some degree of asymmetry. Classical round PNs, which might represent isotropic mass loss, are the minority. Balick (1987) defined several morphological classes based on the outline of the nebular core, such as elliptical and butterfly. Balick argued that a large fraction of PNs have a relatively dense equatorial waistband. Prolate elliptical, bipolar, and closely related nebular geometries develop as a consequence. Manchado et al. (1996a) use the interior symmetry to define classes. The major morphological classes defined by Manchado et al. (2000) are round (R), elliptical (E), bipolar or quadrupolar (B), and pointsymmetric (P) planetary nebulae. Bipolar core (BC) PNs, defined by Stanghellini et al. (1999), are those planetary nebulae characterized by a bi-nebulosity in the core, which may have lobes below detectability.

Bipolar PNs appear to be associated with particularly dense tori or other types of collimation “nozzles” that form as a normal part of their evolution (Balick 1987; Icke, Preston & Balick 1989). Interestingly, Galactic bipolar PNs are located preferentially in the plane—i.e., their scale height (z) distribution is similar to that of Pop I stars initially more massive than about $2 M_{\odot}$. Other less extreme morphological types of PNs have a larger scale height and evolve from less massive progenitors (Stanghellini, Corradi, & Schwarz 1993; Manchado et al. 2000).

Bipolar and other extremely axisymmetric PNs also tend to be enriched in N and O, but relatively depleted in C/O as found, e.g., by Peimbert (1978); Torres-Peimbert

& Peimbert (1997). These results provide important insight into the shortcomings of present models for AGB envelope ejection (Frank 2000). Peimbert (1978); Torres-Peimbert & Peimbert (1997) suggested that convective dredging operates differently in stars of different initial masses, as expected from the models of stellar evolution (van den Hoek & Groenewegen 1997).

Therefore Galactic PNs suggest that initial stellar mass, and, perhaps, local chemical composition determine the outcome of PN abundances and morphologies. The trends found in the Galactic PNs are supported by a sizable collection of data; nonetheless, they suffer two key impediments for this type of study: namely, the long-standing uncertainties in the distances of Galactic PNs and the selection effects due to absorption by interstellar dust.

One important aspect of morphological studies is the dependence of PN morphology on the emission line in which they are imaged. It has been demonstrated that, while generally the $H\alpha$ and $[OIII]$ morphologies nicely represent the overall nebular volume, low-excitation lines such as $[NII]$ emphasize some particularly interesting small-scale morphological features, such as organized ensembles of low-ionization knots and point symmetry and quadrupolarity (Stanghellini, Corradi, & Schwarz 1993; Manchado, Stanghellini, & Guerrero 1996b). A series of narrow-band images of PNs is the ideal database to start answering some of the current questions on the morphology formation mechanisms, and to study morphological types in detail.

Statistical studies of the properties of PN morphologies, masses, luminosities, ionization, and chemical abundances in which selection bias is minimized and uncertainties in distances are eliminated can be pursued in the Magellanic Clouds. However, any comparison of the morphological and stellar properties of Galactic and MC PNs require the spatial resolution of the *HST* in order to resolve the nebulae and to obtain accurate photometry of the central stars in very crowded fields. Using *HST*, MC PNs can be observed with a physical

resolution that is comparable to ground-based observations of typical Galactic PNs.

Since 1999 we have embarked in a large study of MC PN morphologies, evolution, central stars, and progenitors. At this time, several *HST* programs that aim at collecting a very large dataset of STIS slitless spectroscopy and broad band photometry of LMC and SMC PNs have been completed or are active, and other programs are scheduled to be executed in Cycle 10.

This paper presents data from the Cycle 8 *HST* snapshot survey of LMC PNs (program 8271), consisting of a survey of 29 LMC PNs, acquired in broad band imaging and slitless spectroscopy with STIS. The broad band images of these PNs have been already published by Shaw et al. (2001) (hereafter Paper I), with an extensive discussion on PN morphology and evolution for the sample of program 8271 and of other HST archived images of MC PNs. Here we present a study of the monochromatic images of the LMC PN sample, obtained by using STIS slitless spectroscopy. After calibration, the slitless images are functionally the same as calibrated narrow-band filter images since Doppler smearing is insignificant. We discuss the data acquisition strategy and analysis procedures in §2. In §3 we present the images, the integrated spectral line intensities, and surface brightness estimates. Some of the surface brightness results are unexpectedly correlated, so we discuss the data trends and their significance. Finally, in §4, we give a summary of our work so far, and a glance to the future of our extensive Magellanic Cloud Planetary Nebulae project.

2. Data calibration and analysis

2.1. Slitless strategy

The observations presented in this paper are from *HST* GO program 8271, using the Space Telescope Imaging Spectrograph. See Paper I for the observation log, observing

configuration, target selection, acquisition, and basic calibration (through flat-fielding). Paper I also presented, for each nebula, a broad-band image, a contour plot in the light of [O III] $\lambda 5007$, and a discussion of the morphological classification. We present here slitless spectrograms obtained with gratings G430M, covering the range 4818 Å to 5104 Å at 0.28 Å pixel⁻¹, and G750M, covering the range 6295 Å to 6867 Å at 0.56 Å pixel⁻¹. See the STIS Instrument Handbook (Leitherer, et al. 2000) for additional details of the instrument setup. The exposures were planned to obtain a good signal-to-noise ratio in the [O III] 5007 and H α emission lines, but up to eleven additional bright emission lines of varying ionization were detected, including H β and [O III] $\lambda 4959$ using G430M, and [O I] $\lambda\lambda 6300, 6363$, [S III] $\lambda 6312$, [N II] $\lambda\lambda 6548, 6584$, [He I] $\lambda 6678$, and [S II] $\lambda\lambda 6716, 6731$ using G750M. A stellar or nebular continuum was also detected in the spectrograms of some objects.

2.2. One dimensional spectral extraction, and total line intensities

For most nebulae the combination of dispersion and plate scale (0".051 pixel⁻¹) allows a clean separation in the dispersion direction of the monochromatic images for all emission lines. However, if the nebular extent exceeds about 1".4 the H α and [N II] $\lambda 6548$ lines, and the [S II] $\lambda 6716$ and $\lambda 6731$ lines, will overlap. A few of the more extended targets suffered from this overlap, and a two-dimensional line deblending technique was required to solve for the individual narrow-band images (see § 2.3).

We extracted one-dimensional (1D) spectra from the slitless spectrograms for each nebula and applied a photometric calibration using the standard STIS calibration pipeline module **x1d** (McGrath, Busko, & Hodge 1999).

A significant complication when extracting extended objects is to include the majority of the light, while keeping the virtual extraction slit small so as to maximize the

signal-to-noise (S/N) ratio (see Leitherer & Bohlin 1997). The extraction box size for each nebula was chosen to accept most of the flux without compromising the S/N too much, and the background regions were carefully selected to avoid stray stellar spectra in the slitless images. In Table 1 we give the extraction parameters for the nebulae. Column (1) lists the LMC PN name (SMP nomenclature favored when available); columns (2) through (4) give respectively the grating name, the center of the extraction window, and its size.

We measured emission line intensities using the IRAF³ **splot** task, which permits flux measurements even when the intrinsic line profiles are far from instrumental (as they were for most of our targets). We typically use the deblending cursor command of **splot**, even in cases where there is not any obvious blending of emission lines. We prefer this procedure primarily because it automatically estimates the nebular continuum. We typically fit individual gaussian widths for all the lines within a selected region, but we may fit a single gaussian width for multiple lines if we feel that the latter procedure achieves a better overall measurement.

In cases where line profiles are significantly non-gaussian, and also for the very extended objects, we may use the *e* cursor command in the **splot** task. We also use this command to check whether the total flux measured across several lines matches reasonably well with the sum of the individual line fluxes measured with the deblending command. In a case with complex nebular continuum, we may estimate the continuum better by eyeball, and measure it just with cursor clicks, than by a fitting routine.

In Table 2 we report the measured line intensities. Column (1) gives the common

³IRAF is distributed by the National Optical Astronomy Observatory, which is operated by the Association of Universities for Research in astronomy, Inc., under cooperative agreement with the National Science Foundation.

names, Column (2) gives the logarithmic $H\beta$ intensities, not corrected for extinction, in $\text{erg cm}^{-2} \text{ s}^{-1}$; column (3) lists the logarithmic optical extinction at $H\beta$; columns (4) to (14) give the line intensities for each nebula, relative to $H\beta = 100$, not corrected for extinction. The line identifications, which are given in the column headings, were unambiguous in spite of the lack of a wavelength comparison arc since only the most prominent nebular lines are detectable in the spectrograms.

2.3. Two-dimensional spectral extraction

The geometric calibration of the 2D spectra is performed with the STIS calibration pipeline module **x2d**, which produces a rectified 2D spectrum which is linear in both the wavelength and the spatial directions. The output spectrum has units of $[\text{ergs cm}^{-2} \text{ s}^{-1} \text{ \AA}^{-1} \text{ arcsec}^{-2}]$. We used the 2D spectra to measure the 2D line intensity of all detected spectral lines, using the same extraction windows and background offsets as the 1D spectral extraction (see Tab. 1), so the two measurements are readily comparable, and they offer a check on the procedure and on the calibrated image quality.

Two of the angularly largest of our targets, SMP 93 and SMP 59, suffered from severe overlap of the emission lines. For these nebulae it was essential to apply a deblending technique on the 2D spectral images in order to separate the monochromatic images in the $H\alpha$ -[N II] group. We used the following simple procedure:

1. The images were sky-subtracted by using the mean signal within a suitable sky window (see Table 1 for the center and sizes of the extraction windows).
2. We take advantage of the fact that the [N II] lines are identical in shape and have a fixed intensity ratio. This allows us to use the redward, uncontaminated portion of $\lambda 6584$ line to subtract from the blend at the position of the $\lambda 6548$ line; likewise the

uncontaminated blueward portion of the [N II] $\lambda 6548$ line was used to subtract from the blend at the position of the $\lambda 6584$ line, leaving an uncontaminated $H\alpha$ image.

3. We obtain the uncontaminated [NII] image by subtracting the reconstructed $H\alpha$ image from the entangled image group.

A check on the quality of the above procedure has been performed by comparing the total flux of the $H\alpha$ plus [N II] blend with the sum of the flux from the blend as measured with the 1-D technique. The agreement is good at least to the 10% level in the PNs analyzed in this paper. However, it is clear that the technique is far from perfect: the relative intensities for $H\alpha$ for both SMP 93 and SMP 59 is much less than what is possible for a nebular gas. Our technique undoubtedly fails to assign the correct total flux in these line, and we report only the sum of the $H\alpha$ and [NII] intensities in Table 2. Furthermore, data relative to these two PNs will not be entered in the diagnostic plots of this paper, wherever the extinction corrected fluxes are used.

For SMP 59 and SMP 93, the [SII] $\lambda 6716$ - 6731 lines are also superimposed in the dispersion direction. In this case, since the line ratio is not known (it depends on the electron density) we measure the line blend, and give it in Table 2.

2.4. Error analysis

The 1D and 2D intensities can be compared to make a detailed analysis of the errors in our measurements. The intensities for a given emission line and nebula should be the same no matter the method used for the analysis. On the other hand, we should limit this comparison to the nebulae whose images do not overlap in the dispersion direction. We calculate the normalized difference between 1D and 2D measurements as $\Delta_{1D-2D} = (F_{1D} - F_{2D})/F_{1D}$ for each spectral line and each PN in our sample. We plot

Δ_{1D-2D} against the 1D flux in Figure 1. We find that the difference depends strongly on the observed line intensity. In particular: $|\Delta_{1D-2D}| < .05$ if $\log F > -12.25$, $|\Delta_{1D-2D}| < .15$ if $-12.25 < \log F < -12.75$, $|\Delta_{1D-2D}| < .2$ if $-12.75 < \log F < -13.5$, $|\Delta_{1D-2D}| < .25$ if $-13.5 < \log F < -14.5$, and finally $|\Delta_{1D-2D}| < .55$ if $\log F > -14.5$. The only exception to these results are a handful of data points in the $-13.5 < \log F < -14.5$ interval. These are the [N II] $\lambda 6584$ lines that may be blended with the $H\alpha$ lines, even for relatively small objects (e. g., SMP 10 and SMP 100), and another couple of lines whose measurements have very high errors (the [O I] $\lambda 6363$ line in SMP 78 and SMP 9, and the He I $\lambda 6678$ line in SMP 81).

We have also examined the variance of Δ_{1D-2D} with respect to the nebular radii, to find that there is no dependence of the error in the flux measurements to the size of the nebula, nor on the morphological type. We conclude that the errors listed above, in relation to the intensity of the 1D spectral lines, are the formal internal observational errors for the fluxes presented in this paper.

In order to asses the quality of our data, and the improvement over the published line intensities, we have compared the measured MC PN intensity ratios of Table 2 to the fluxes published by Vassiliadis et al. (1992), Meatheringham & Dopita (1991a), and Meatheringham & Dopita (1991b). In all, we found published fluxes for 15 of 29 planetaries. The line intensities from Meatheringham & Dopita (1991a) and Meatheringham & Dopita (1991b) are corrected for extinction, so it was necessary to apply the reddening function before comparing them to our data. To this end, we use the extinction constants given by the individual references, and average Galactic reddening curve of Savage & Mathis (1979), which is reliable at these wavelengths even for the LMC (Howarth 1983). In Figure 2 we show the comparison between our line intensity ratios and those from the references above. The intensity ratios are plotted in logarithmic form, to allow the simultaneous view

of low and high fluxes. The correspondence of our intensities to the ones in the literature is generally good, and typically within the observing errors quoted in the references (indicated with vertical lines on the plot). The notable exceptions are the [N II] 6548 lines of SMP 10 and SMP 100, overestimated in the references (the dots in the middle of Fig. 2). We believe that our [N II] measurements for these two nebulae are more reliable than those by the literature source (Vassiliadis et al. 1992). In fact, we know that the [N II] 6584/6548 ratio should be approximately 3 (Osterbrock 1989), and our ratios are 2.96 and 2.98 respectively for SMP 10 and SMP 100, while the ratios from Vassiliadis et al. (1992) are 11.4 and 11.1 respectively. The errors in the reference may be caused by the poor separation of the [N II] and $H\alpha$ lines in the dispersion direction. Vassiliadis et al. (1992), for example, use a bandpass of FWHM 16 Å to observe the $H\alpha$ lines, and this separation may be not enough for SMP 10 and SMP 100, where the [N II] lines have low intensity.

A close inspection of Figure 2 reveals a small discrepancy in the [O III] $\lambda\lambda 4959, 5007$ line intensities (the clump of dots at $\log F \approx 2.5$). The source of the mismatch may lie in a difference in the $H\beta$ fluxes, which are used to scale the intensities and which are often weakly exposed in our spectrograms for larger nebulae. The ultimate cause of the discrepancy may lie with a systematic problem in the flux calibration for the STIS CCD. Stys & Walborn (2001) found that an apparent degradation in the sensitivity of the STIS CCD with time (which is not yet corrected in the calibration pipeline) may in fact have its root cause in a degradation of the CCD charge transfer efficiency. While not yet well characterized for the grating/central wavelength combinations used here, in general the effect is that charge lost during the CCD readout is manifested as lower measured fluxes. Depending upon the brightness of the surrounding mean sky and the number of detected counts per pixel of the emission feature, the effect could range from less than a percent to as much as 15% (Stys & Walborn 2001) for the emission lines reported here. We anticipate that the effect for the $H\beta$ fluxes (and hence the scaling for all of the emission lines) for

angularly large nebulae is likely in the range of 1–3%. The effect on the very weakest lines (such as [O I]) in large nebulae may approach 10%, but the effect on well exposed lines in small nebulae is likely negligible.

3. Results

3.1. Nebular morphology in various lines

The calibrated slitless images of all but the very largest LMC PNs are shown in Figure 3. For each nebula we show the [OIII] 5007 Å section of the G430M spectra, when available, and the H α and [NII] line group section of the G750M spectra. The images of SMP 94 are not shown in Figure 3, because we are convinced this object is not a PN, based on its spectral structure (see Paper I). The slitless images for the two largest nebulae are shown in Figure 4, where we show the [OIII] 5007 Å images, the H α and [NII] group, and the [NII] images as reconstructed with the algorithm described in §2.3.

Paper I describes the morphology of our sample nebulae in detail. In the following we limit the description to interesting morphological features of the spectra that have not been mentioned in Paper I. Morphological types are taken from Paper I unless stated otherwise. As in the other papers of this series, we use the Manchado et al. (1996a) morphological classification scheme, and we also add the *bipolar core* class. Hereafter, when we refer to **symmetric** PNs we include E and R *without* a detected bipolar core, and with **asymmetric** PNs we indicate the bipolar and quadrupolar (B), and the bipolar core (Rbc and Ebc) PNs. We keep pointsymmetric PNs outside these groups.

- J 41: The nebular morphology is Ebc. It is observed only with the G750M configuration, and only the H α emission is detected. No low-ionization structures (hereafter “LIS”) are seen in this object.

- SMP 4: The nebular morphology is E. This attached halo multiple shell PN shows its morphology in all the detected lines. This is shown for [OIII] $\lambda 5007$ Å and $H\alpha$ in Figure 3, and it is also true for $H\beta$ and [OIII] $\lambda 5007$ Å. The emission in the [NII] lines was marginally detected below the 3σ level. No LIS’ are seen in this object.
- SMP 9: The nebular morphology is Ebc. The barrel shape is shown in all detected emission lines, including [NII] . No LIS’ are seen.
- SMP 10: The nebular morphology is P. The [NII] emission occurs only in the *arms* of this PN. There are three distinct morphological features: an inner ellipse (not visible in [NII]), a round edge-brightened mantle that surrounds it, and two “spiral arms” that are most prominent in [NII] . We note that the enhanced emission that defines the inner ellipse is oriented such that the major axis is aligned with the *arm* structure in the outer nebula. It is conceivable that this feature traces more subtle, unresolved structure such as a jet from the central star that terminates at the ends of the arms, similar to the Cat’s Eye nebula (NGC 6543). Note that the photometric radius measured by Shaw et al. (2001) on the [OIII] image is very close to a photometric radius measured on the [NII] image. Although this nebula is rather extended, none of 2D the spectral lines overlap.
- SMP 13: The nebular morphology is Rbc. The same patchy morphology is visible in all detected lines. The [NII] emission (see Fig. 3) is very faint except along the lobe edges where its structure is clumpy. This behavior is characteristic of Galactic bipolar PNs such as NGC 2346 and NGC 6537, which are similar in appearance to SMP 13. In the spectral data we can see a faint stellar spectrum that could be associated with the central star.
- SMP 16: The nebular morphology is B. This very prominent bipolar shows its morphology in all detected lines. As mentioned in Paper I, the [NII] emission reveals

a knotty character of the lobes, marginally evident in Fig. 3. No LIS' are seen in this object.

- SMP 18: The nebular morphology is Rbc. A central cavity of this multiple shell PN may not be evident in Fig. 3, but it is obvious in the frame. The faint stellar spectrum seen in Fig. 3 may be associated with the central star.
- SMP 19: The nebular morphology is Ebc. The nebula reminds us of a barrel seen in projection. Small protrusions may emerge from the barrel along its symmetry axis, much like NGC 40. No LIS' are seen.
- SMP 25: The nebular morphology is R. The nebula appears amorphous in this logarithmic display. No LIS' are seen.
- SMP 27: The nebular morphology is Q. This interesting quadrupolar PN has the central star spectrum easily seen both in the G430M and G750M observations. The [NII] emission has very low surface brightness.
- SMP 28: The nebular morphology is P. The *arms* seen in the [NII] image are too thin to be reproduced in Figure 3. The shape may be similar to that of SMP 10.
- SMP 30: The morphological type is irregular, possibly B. The characteristic of this PN is the very high [NII] intensity at the nebular edges. The [NII] images give much more information on the nebular morphology than the H α or [OIII] images, defining knots and arcs.
- SMP 31: The nebular morphology is possibly R. A central star is not seen in the clear image, but there is hint of the stellar continuum in the slitless spectra. No LIS' are seen.

- SMP 34: The nebular morphology is E. A different morphology is detected in the [NII] lines. Although these lines are faint, a hint of a bipolar shape is shown. No LIS' are seen.
- SMP 46: The nebular morphology is Ebc. A central cavity is particularly clear in [NII] . No LIS' are seen.
- SMP 53: The nebular morphology is E, possibly Ebc. A ringlike structure is clearly seen in the [NII] emission lines. Filamentary LIS' surround the core, something like SMP 30.
- SMP 58: The nebular morphology may be R. A barely resolved PN, the central star spectrum is seen in the G750M slitless observations (see Fig. 3). An emission feature at about 6577Å is probably stellar. No LIS' are seen.
- SMP 59: The nebular morphology is probably Q. A spectacular PN, its morphology is particularly evident in the [NII] emission lines. The reconstructed [NII] image in Fig. 4 shows that there may be multiple emission or knots in this nebula.
- SMP 65: The nebular morphology is R. No LIS' are seen.
- SMP 71: The nebular morphology is E. No LIS' are seen.
- SMP 78: The nebular morphology is Ebc. No LIS' are seen.
- SMP 79: The nebular morphology is Ebc. Ringlike structures are evident in the [NII] emission. No LIS' are seen.
- SMP 80: The nebular morphology is R. Ringlike structures are evident in the [NII] emission, and the central star spectrum is seen in the slitless observations with the G750M grism.

- SMP 81 is not shown in Figure 3 for lack of interesting extended features. The nebular morphology is probably R. An extremely faint, marginally detected central star spectrum is seen in the G750M slitless observations.
- SMP 93: The nebular morphology is B. The best way to study the morphology of this spectacular bipolar PN is to look at the [NII] reconstructed image of Fig. 4. The central ring and the lobes are enhanced at this wavelength. The morphology of the H α emission looks similar to that of the [OIII] emission. The edges of the main morphological structures are low in emission, much like most Galactic PNs. NGC 6445 is similar in structure to SMP 93.
- SMP 94: The nebular morphology is unresolved. We believe that this object is not a PN (see the discussion in Paper I). Although we include the line flux analysis in Table 2 for SMP 94, we do not include it in the Figures, not in the following analysis and related plots.
- SMP 95: The nebular morphology is Ebc. Faint low-ionization ansae can be seen in [NII] .
- SMP 100: The nebular morphology is Ebc, or Q. The [NII] emission lines show the knots’ outline of this interesting PN. No LIS’ are seen.
- SMP 102: The nebular morphology is R, possibly bc. The interior shows a round clumpy ring. The brightest of the knots is faintly visible in [NII] .

From the above analysis we note that, while the morphological type is more or less the same in all detected lines for most PN, the morphologies are sometimes more evident in the low-ionization images, as if these arise primarily along the nebular border. Some distinct, compact emission features are seen most prominently in [NII] .

3.2. The surface brightness-radius correlation

In Paper I we found a tight correlation between [OIII] $\lambda 5007$ Å surface brightness (hereafter SB, defined to be the integrated line intensity divided by the nebular area πR_{phot}^2) and nebular photometric radius R_{phot} which appears to be independent of morphological type or other properties of the targets. Here we extend these studies to other bright emission lines in order to see how the correlation depends on the nebular ionization state, abundances, or other parameters. In the discussion below we consider the [OIII] and [SIII] lines to arise in the nebular zone of moderate ionization, [NII] and [SII] to arise in zones of low ionization, $H\alpha$ and $H\beta$ to arise in both zones, and [OI] to arise in an excited neutral zone at the nebular boundary.

In Figure 5 we plot \log SB against $\log R_{\text{phot}}$ (the physical photometric radii) for each of the representative emission lines of our nebulae (except [SII] which are presented in Figure 6 and discussed later). All surface brightnesses have been corrected for extinction using the extinction constants of Table 2 and the Galactic extinction curve (see § 2.3). Note the consistency in the trends from one line to another, with the exception of [NII], where the overall relation is hidden by scatter. The reason for the scatter is that the bulk of the [NII] emission often arises in the nebular interior – in the same zone – where the [OIII] lines arise, whereas in other cases the [NII] lines arise at the nebular boundary, or in the LIS'. This means that the plot of the surface brightness decline in the [NII] line is related not only to the evolution of the gas, but also to the ionization effects. Note that the most discrepant points are relative to asymmetric PNs. The agreement of the [OI] line SB vs. R_{phot} correlation with [OIII] and $H\alpha$ plots is the big surprise: [OI] should arise only at the nebular boundary, and still it declines with R in a similar fashion as the [OIII] lines.

In Figure 5 we superimpose lines describing the $SB \propto R_{\text{phot}}^{-3}$ relation, the best eye-fit to the data for all emission line plots. Once again we see that the trends are tight, and

the trends seem to be independent of the nebular state or morphology. By examining the $\text{SB}-R_{\text{phot}}$ trends for each morphology type we see that while the SB trend is the same for all morphological types, asymmetric PNs are located in the bottom right part of the relation, indicating their evolved status. A similar result, but for the $[\text{OIII}]$ line only, was derived in Paper I⁴

The relations above hold only in the cases in which the nebular density N_e is smaller than the critical density, N_{crit} (the density at which the collisional de-excitation rate balances the radiative transition rate). We have calculated the critical density for the ions considered in Figure 5, by using the **nebular** routines (Shaw & Dufour 1995), to prove that $N_e \leq N_{\text{crit}}$ for all the PNs for the ions examined in the Figure.

Let us now examine the cases in which the electron density of the PNs is higher than the critical density. In Figure 6 we plot the usual $\log \text{SB}$ vs. $\log R_{\text{phot}}$ relation, in the light of $[\text{SII}]$. The critical densities are respectively $N_{\text{crit}} \sim 13.6 \times 10^3 \text{ cm}^{-3}$ for the transition from level 2 to level 1 (6731 Å line), and $N_{\text{crit}} \sim 11.4 \times 10^3 \text{ cm}^{-3}$ for the transition from level 3 to level 1 (6716 Å line). We have compared these critical densities with the electron density of the PNs, and plotted with filled symbols in Figure 6 (we do not code for morphological type in this Figure, to avoid confusion) the PNs in which $N_e \geq N_{\text{crit}}$. We can infer that a simple surface brightness versus photometric radius relation does not hold for the majority of the objects, in this line.

⁴Note that the upper left panel of Figure 5 is not identical to the $\log \text{SB}-\log R_{\text{phot}}$ Figure of Paper I, for two reasons. First, in Paper I we added in the Figure all data from the archived LMC PNs as well, while here we restrict the discussion to the data of our program 8271. Second, in Figure 5 we updated all the line intensities, and relative surface brightness, by using our own HST fluxes from Table 2.

On the other hand, most nebulae are less dense than the critical density for the [SII] $\lambda 6716\text{\AA}$ line, and a sizable fraction of them are less dense than the critical density for the [SII] $\lambda 6731\text{\AA}$ line. This effect explains the different relation observed.

3.3. Electron density and ionized masses

Nebular densities N_e of the 12 MC PNs with the brightest [SII] lines were estimated using the IRAF package **nebular** and assuming an electron temperature of 10^4 K. The electron densities calculated in this way are reliable only for the density interval between 300 and 7000 cm^{-3} (Stanghellini & Kaler 1989). The $\log N_e - \log R_{\text{phot}}$ is shown in Figure 7. Morphological types are plotted with different symbols. Based on a small and selected sample, the densities of MC PNs are not related to their morphologies.

If all PNs have the same mass, morphology, expansion rate, and density boundedness (i.e., ultraviolet opacity) then we would expect a tight negative correlation between density and radius. We see only a loose correlation, if any at all. This is no surprise. The same absence of a tight density–radius correlation was seen earlier by Dopita & Meatheringham (1990) based on ground-based data.

The ionized masses have been calculated from the [SII] densities and the photometric radii using the methodology of Boffi & Stanghellini (1994). This method assumes spherical geometry and uniform density within the filled parts of the nebula, which is obviously the exception and not the rule (Figs. 3 and 4), but does not assume a value for the filling factor (ϵ) of the nebulae (Boffi & Stanghellini 1994). Implicit also is the assumption that the [SII] densities are characteristic of the entire nebula, whereas we have seen that knotty and filamentary LIS’ sometimes dominate the [NII] and [SII] emission.

We find that the average ionized mass is 0.21 M_{\odot} , the same that has been found

by Boffi & Stanghellini (1994) from a larger LMC PN sample, albeit without diameters measured directly from deep *HST* images. The ionized masses for the only bipolar and elliptical PNs in our sample with reliable electron density are respectively $0.33 M_{\odot}$ and $0.17 M_{\odot}$. Barlow (1987) used the [OII] electron density to derive the ionized mass of 32 Magellanic Cloud PNs, and they found an average mass of $0.25 \pm 0.17 M_{\odot}$ for the complete sample, and $0.39 \pm 0.22 M_{\odot}$ for the type I PNs within their sample. Our results are thus in agreement with those of Barlow (1987), including a possible ionized mass offset between PN types, type I PNs and bipolar PNs being the more massive ones. A much larger data set is needed to confirm these trends.

The ionized mass versus radius logarithmic relation is plotted in Figure 8 using the same symbol definitions as in Figure 7. The tight correlation found for Galactic PNs (Boffi & Stanghellini 1994) is not found in this plot of LMC PNs, where the two (logarithmic) variables have a low correlation coefficient of 0.35. Much of this scatter is the result of inappropriate assumptions such as spherical symmetry, constant density, and accurate nebular radii. The assignment of a nebular radius is especially treacherous for bipolar PNs with open, slowly fading lobes along the major axis and bright, sharp and closely spaced edges along the minor axis.

3.4. Nebular excitation

In planetary nebulae, one measure of stellar evolutionary state is nebular excitation, which tracks the evolution of the temperature of the central star. For ionization bounded nebulae this can be gauged from the relative volumes of regions dominated by He° , He^{+} and He^{++} . Nebular excitation is best measured using ratios of recombination lines of H and He which are only slightly affected by electron temperature T_e . The signal-to-noise and restricted bandwidths of our spectra render this impractical.

We use an alternate measure of excitation, $EC = (I_{[O\ III]5007} + I_{4959})/I_{H\beta}$. The ratio is sensitive linearly to the fraction of O^{++}/O (much like He^+/He) and exponentially to the electron temperature T_e . The fractional ionization of O^{++} varies as the star evolves: over time the dominant stages of oxygen ionization first rises very quickly from O^+ and then very slowly to O^{+++} . Similarly T_e tends to increase with time as the average kinetic energy of photoionized electrons rises with stellar surface temperature. As the central star evolves from 25,000 K to over 10^5 K, EC will rise. Afterwards, when the star begins to fade and lower its temperature, the EC will begin to fall. Overall, however, EC is a decent estimator of stellar temperature.

The measured photometric radius, R_{phot} should be a good measure of age because the nebula expands. But it is far from perfect. Different rates of expansion in different PNs will introduce scatter into the use of R_{phot} as an age indicator for a group of PNs (see Paper I).

Since round and elliptical PNs seem to evolve from progenitors of lower mass than bipolar and bipolar core PNs (see Stanghellini et al. 2000) we might expect to find correlations in EC and R_{phot} separately for various morphological types. Figure 9 is a plot of EC vs R_{phot} for LMC PNs. It shows a good correlation for asymmetric PNs (the squares and triangles, see the caption) and scatter for other types. We find small low-excitation objects and relatively large high-excitation R and E PNs, as expected. The scatter associated with these objects could be related to the different rates at which they expand as well as a bias against the discovery of large, low-SB PNs.

Figure 10 is a plot of EC vs $\log SB\ [OIII]$ for LMC PNs. The interpretation of the plot is complex and limited by the small sample size. Assuming that all asymmetric (squares and triangles) PNs were formed with a similar O/H ratio it follows that they show a clear correlation independent of their initial oxygen abundances. On the other hand, no correlation is seen for R and E PNs. There is a bias against the discovery of large R and

E PNs owing to their very low surface brightnesses. But most of all we believe that the fraction of escaping ultraviolet radiation increases drastically for R and E PNs. Variations in mass or expansion speed will tend to introduce scatter into SB for a group of PNs.

The $H\alpha$ recombination-line luminosity of an expanding PN is a measure of the rate at which ionizing photons are being absorbed in the nebula. We expect the $H\alpha$ flux to be constant while the nebula is ionization bounded and to drop thereafter until the star itself drops in UV photon emission rates late in its life. In Figure 11 we plot the $H\alpha$ line luminosity, corrected for extinction, against EC. Since all PNs in this plot are at the same distance, the $H\alpha$ intensity is proportional to the stellar luminosity. Note that in Figure 11 the excitation constant increases from right to left in the plot, as does the effective temperature in the HR diagram.

Dopita & Meatheringham (1990) have used a similar diagram to compare the observed LMC and SMC PNs with simple evolutionary models. The novelty of our approach is that we added the information on nebular morphology. In Figure 11 we can follow the PN evolution in *two dimensions*, exactly as we follow the stellar evolution in the HR diagram. We can see the simultaneous effects of changes in the effective temperature (through the parameter EC) and of the luminosity (through the $H\alpha$ brightness) for different nebular morphologies. PNs evolve first from right to left (and from bottom to top) as their central stars get hotter and their shells get thinner, then from top left to bottom right as the central stars evolve in the cooling line, at constant radii.

Naturally, much modeling is needed before we could derive a quantitative conclusion from Figure 11, but we feel that the empirical result is very strong, that is, most of the observations of asymmetric PNs in the LMC are consistent with them being on the *cooling sequence*, beyond the central star’s temperature maxima. The opposite is true for symmetric PNs. This observational result is consistent with our other findings that relate

asymmetry with higher progenitor mass, in this case it looks like also the post-AGB stellar mass is higher for asymmetric PNs. Our future study on the central star’s photometry will clarify some of the open questions posed by these diagrams, and appropriate hydrodynamic modeling will complete the description of the evolution of PN in the LMC.

3.5. Nebular extinction

We analyzed the extinction in this sample of nebulae to look for evidence of internal dust, and for any variations with morphological type. Ciardullo & Jacoby (1999) reported evidence of a correlation of extinction with the mass of the central star for PNs in the Magellanic Clouds and in M31. We examined some nebulae in our sample to look for spatial variations in the extinction, which we believe would be a strong indicator of the presence of dust internal to the nebulae. We took ratios of the $H\beta$ and $H\alpha$ images for PNs where the extinction constant was relatively high, or that had morphological features that can be associated with the presence of internal dust, such as the pinched waist of the bipolar nebulae SMP 16 and SMP 30. In no case did we find significant spatial variations in $H\beta/H\alpha$, at least on spatial scales of ~ 0.04 pc. We note, however, that many of the PNs with high extinction are angularly small, and furthermore the S/N ratio of our $H\beta$ images is often not high. Still, for nebulae within our sample that lend themselves to this analysis, the internal extinction, where present, must be spatially uniform on small spatial scales.

Another way to address the question of whether the extinction is internal to the nebulae is to examine whether it declines with nebular physical radius, as might be expected if internal dust were either destroyed or geometrically diluted as the nebula expands. We plot in Figure 12 the nebular extinction constant vs. the log of the physical radius for all nebulae in this sample, and we also include the PNs in the archived sample by Dopita (HST program 6407, see also Paper I). The Figure shows that the amount of extinction

does not depend on morphological type, except possibly for large bipolar nebulae where c is generally low. It also shows that the amount of extinction depends only weakly on physical size, in that nebulae smaller than 0.1 pc suffer at least some extinction. This question should be examined again with a larger data set, but for now the safest conclusion is that the extinction for PNs in this sample spans a large range at all sizes and does not depend strongly, if at all, on morphological type. Stanghellini, et al. (2000) showed for Large Magellanic Cloud PNs that bipolar (and bipolar-core) morphology correlates with chemical properties that are related to higher-mass central stars. Yet the absence here of any relation between bipolar morphology and extinction, and the lack of internal variation in extinction on modest spatial scales, suggests that there is no clear relationship between internal nebular extinction and central star mass. The lack of nebulae smaller than 0.1 pc with zero extinction may indicate the presence of dust within these nebulae; our spatial resolution is insufficient to search for spatial variations in extinction. It would be worthwhile to observe these nebulae in the thermal infrared to examine the dust properties more thoroughly. In any case, we find no evidence that internal extinction in LMC PNs varies with central star core mass.

4. Discussion

In this paper we have shown the STIS slitless observation of a group of 29 LMC PNs, and analyzed the spectroscopic data. The images of Figures 3 and 4 present an unique data set that includes a wealth of morphological and spectral information. The line intensities measured from the slitless spectra, although limited to the brightest spectral lines in the observed wavelength windows, represent some of the best quality spectral data for the LMC PNs. By adding spatial information to the spectrograms, we are able to determine an accurate morphology, where the effects of the ionization structure are fully understood. Our

comparison of the 1D to the 2D line fluxes helps us to characterize our internal consistency, while the comparison to published data reveals the high photometric quality of these data

The nebular emission at the different wavelengths has been analyzed in various ways. We obtain the following results.

1. While the $H\alpha$ and $[OIII]$ lines are perfect for morphological studies of the main body of the PNs, the $[NII]$ emission lines are ideal to detect knots, ansae, and other deviation from symmetry, not always detectable in the $H\alpha$ light, and to clarify the morphological classification.
2. The surface brightness relation with the photometric nebular radius is indistinguishable for all the observed lines where the nebular electron density is smaller than the critical density, and with the exception of the $[NII]$ lines. The very tight, universal $\log SB \propto -3 R_{\text{phot}}$ relation indicates the nebular evolution. Such a relation could be used to calibrate the Galactic PN distance scale.
3. The marginal correlations between the photometric radii and the electron densities and the ionized nebular masses indicate that the spherical approximation is wrong for the LMC PNs, and that assuming that all PNs have the same ionized mass is very misleading. We found that the average ionized mass for our sample is $0.21 M_{\odot}$. A marginal correlation between asymmetry and high ionized mass was detected.
4. The $[OIII]$ to $H\beta$ line ratio is a good measure of the nebular excitation. We find that there is a tight correlation between EC and size in asymmetric PNs, suggesting that these nebulae are on a faster evolving track. This result is in agreement with our previous results of Paper I, and Stanghellini, et al. (2000), that observations of asymmetric LMC PNs are in accord with a rapidly evolving, more massive progenitor, younger generation planetary nebula sequence, compared to the low mass, slow

evolving, round PNs.

5. The internal extinction of the observed nebulae is generally low, and does not depend markedly on morphological type. We find no evidence for a relation between the progenitor mass indicators and the extinction of the nebulae.

In the future, we plan to extend this analysis to our other data samples, the SMC PNs that have been observed in Cycle 9, and an expanded LMC data set that is being collected at the time of writing. At the same time, for the dataset presented in this paper, we will also extract the information about the central stars of those PNs. Eventually we will relate the stellar and nebular properties of all the samples in study.

While most of the results presented in this paper (especially from points 2 and 4 above) need extensive nebular modeling to be understood, their empirical value is nonetheless remarkable. We confirm, with this work, the importance of slitless spectroscopy for maximizing the rate of useful information of these objects. Our future plans include hydrodynamical modeling of the SB vs. R_{phot} relation to test its physical meaning, and to assess its validity as a tool to build the LMC based PN distance scale. We have much to understand about the shape and universality of this relationship which may be useful for PN distances as the period-luminosity relationship for Cepheid variable stars.

Our Web page, <http://archive.stsci.edu/hst/mcpn/>, includes many of the published data and data analysis, and it is a part of the Hubble Data Archive.

This work was supported by NASA through grant GO-08271.01-97A from Space Telescope Science Institute, which is operated by the Association of Universities for Research in Astronomy, Incorporated, under NASA contract NAS -26555. We thank an anonymous referee for an essential suggestion.

Fig. 1.— Comparison of the 1D to the 2D line intensity measurement from our *HST* data. We plot Δ_{1D-2D} against the logarithmic 1D flux for all nebulae of our sample and for all available lines. We do not plot data for those nebulae whose lines overlap in the dispersion direction, see text.

Fig. 2.— Comparison of the measured line intensity ratios with those in the literature, in logarithmic scale. The vertical lines represent the minimum errorbars for the reference fluxes.

Fig. 3.— [OIII] ,H α , and [NII] images of the program nebulae (all PNs except SMP 59 and SMP 93).

Fig. 4.— [OIII] ,H α , and [NII] images of SMP 59 and SMP 93.

Fig. 5.— Surface brightness decline for the mutliwavelength images of the PNs in our STIS survey. Emission lines for which the SB is derived are indicated in the panels. Symbols indicate morphological types: open circles= round, filled circles= pointsymmetric, stars= elliptical, filled triangles=bipolar core, filled squares= bipolar (and quadrupolar) planetary nebulae. The photometric radii are measured from the [OIII] $\lambda 5007$ Å images (see text).

Fig. 6.— The log SB vs. log R_{phot} relation for the [SII] lines. Filled symbols: PNs with $N_e \geq N_{\text{crit}}$, for [SII] 6716 Å (left panel) and [SII] 6731 Å (right panel). Points are not coded for morphology, to avoid confusion.

Fig. 7.— Logarithmic electron density from the [SII] doublet vs. log R_{phot} .

Fig. 8.— Logarithmic ionized mass vs. log R_{phot} .

Fig. 9.— Excitation constant, as defined in the text, plotted against the logarithmic photometric radius.

Fig. 10.— Logarithmic [OIII] surface brightness vs. excitation constant.

Fig. 11.— Logarithmic $H\alpha$ line intensity vs. excitation constant.

Fig. 12.— Logarithmic extinction at $H\beta$ $\lambda 4861$ vs. $\log R_{\text{phot}}$.

REFERENCES

- Balick, B. 1987, AJ, 94, 671
- Barlow, M. J. 1987, MNRAS, 227, 161.
- Boffi, F. R., & Stanghellini, L. 1994, A&A, 284, 248
- Ciardullo, R., & Jacoby, G. H. 1999, ApJ, 515, 191
- Dopita, M. A., & Meatheringham, S. J. 1990, ApJ, 357, 140
- Meatheringham, S. J., & Dopita, M. A. 1991a, ApJS, 75, 407
- Meatheringham, S. J., & Dopita, M. A. 1991b, ApJS, 76, 1085
- Frank, A. 2000, ASP Conf. Ser. 199: Asymmetrical Planetary Nebulae II: From Origins to Microstructures, 225
- Icke, V., Preston, H. L., & Balick, B. 1989, AJ, 97, 462
- Howarth, I. D. 1983, MNRAS, 203, 301
- Leitherer, C., & Bohlin, R. C. 1997, STIS Instrument Science Report 97–13 (Baltimore: ST ScI)
- Leitherer, C., et al. 2000, STIS Instrument Handbook, Version 4.0 (Baltimore: ST ScI)
- McGrath, M. A., Busko, I., & Hodge, P. E. 1999, STIS Instrument Science Report 99–03 (Baltimore: ST ScI)
- Manchado, A., Guerrero, M., Stanghellini, L., & Serra-Ricart, M. 1996a, The IAC Morphological Catalog of Northern Galactic Planetary Nebulae (Tenerife: Instituto de Astrofísica de Canarias)

- Manchado, A., Stanghellini, L., & Guerrero, M. A. 1996b, *ApJ*, 466, L95
- Manchado, A., Villaver, E., Stanghellini, L., & Guerrero, M. A. 2000, *ASP Conf. Ser.* 199: Asymmetrical Planetary Nebulae II: From Origins to Microstructures, 17
- Osterbrock, D. E. 1989, *Astrophysics of Gaseous Nebulae and Active Galactic Nuclei* (Mill Valley, CA: University Science Books)
- Peimbert, M. 1978, *IAU Symp.* 76, ed. Y. Terzian, Reidel, 215
- Torres-Peimbert, S., & Peimbert, M. 1997, *IAU Symp.* 180, eds. H. Habing and H. Lamers, Kluwer, 175
- Savage, B., & Mathis, J. 1979, *ARA&A*, 17, 73
- Shaw, R. A. & Dufour, R. J. 1995, *PASP*, 107, 896
- Shaw, R. A., Stanghellini, L., Mutchler, M., Balick, B., & Blades, J. C. 2001, *ApJ*, 548, 727 (Paper I)
- Stanghellini, L., & Kaler, J. B. 1989, *ApJ*, 343, 811
- Stanghellini, L., Corradi, R. L. M., & Schwarz, H. E. 1993, *A&A*, 279, 521
- Stanghellini, L., Blades, J. C., Osmer, S. J., Barlow, M. J., & Liu, X.-W. 1999, *ApJ*, 510, 687
- Stanghellini, L., Shaw, R. A., Balick, B., & Blades, J. C. 2000, *ApJ*, 534, L167
- Stys, D. J., & Walborn, N. R. 2001, *STIS Instrument Science Report 2001–01R* (Baltimore: ST ScI)
- van den Hoek, L. B., & Groenewegen, M. A. T. 1997, *A&AS*, 123, 305
- Vassiliadis, E., Dopita, M. A., Morgan, D. H., & Bell, J. F. 1992, *ApJS*, 83, 87

Table 1. Spectrum Extraction Parameters

Nebula	Grating	Ap. Center	Ap. Size
		(pix)	(pix)
(1)	(2)	(3)	(4)
J 41	G750M	517	23
SMP 4	G430M	542	30
	G750M	537	30
SMP 9	G430M	521	20
	G750M	517	20
SMP 10	G430M	526	55
	G750M	527	55
SMP 13	G430M	531	27
	G750M	526	27
SMP 16	G430M	517	53
	G750M	514	53
SMP 18	G430M	553	27
	G750M	548	27
SMP 19	G430M	521	25
	G750M	517	25
SMP 25	G430M	511	15
	G750M	506	15
SMP 27	G430M	539	23
	G750M	535	23
SMP 28	G430M	503	12
	G750M	508	23
SMP 30	G430M	528	51
	G750M	525	51
SMP 31	G430M	513	23
	G750M	508	11
SMP 34	G430M	518	23
	G750M	514	20
SMP 46	G430M	538	23
	G750M	533	23
SMP 53	G430M	521	25

Table 1—Continued

Nebula	Grating	Ap. Center (pix)	Ap. Size (pix)
(1)	(2)	(3)	(4)
	G750M	516	25
SMP 58	G430M	521	23
	G750M	516	23
SMP 59 ^a	G430M	521	25
	G750M	516	25
SMP 65	G430M	521	25
	G750M	516	25
SMP 71	G430M	521	23
	G750M	516	23
SMP 78	G430M	521	23
	G750M	516	23
SMP 79	G430M	521	23
	G750M	516	23
SMP 80	G430M	521	15
	G750M	516	15
SMP 81	G430M	521	23
	G750M	516	11
SMP 93 ^a	G430M	521	25
	G750M	516	25
SMP 94	G430M	521	23
	G750M	516	11
SMP 95	G430M	521	27
	G750M	516	27
SMP 100	G430M	521	43
	G750M	516	45
SMP 102	G430M	521	29
	G750M	516	29

^aLarge angular size of nebula requires 2-D extraction; see text.

Table 2. Relative Emission Line Intensities of LMC Planetary Nebulae

Nebula	$F(\text{H}\beta)$ (4861)	c (3)	[OIII] (4959)	[OIII] (5007)	[OI] (6300)	[SIII] 6312	[OI] 6363	[NII] (6548)	H α (6563)	[NII] 6584	HeI 6678	[SII] (6716)	[SII] (6731)
(1)	(2)	(3)	(4)	(5)	(6)	(7)	(8)	(9)	(10)	(11)	(12)	(13)	(14)
J 41		0.00											
SMP 4	−13.55	0.12	452.6	1354.4	312.6
SMP 9	−13.43	0.22	313.7	933.0	38.3	6.5	11.0	62.2	340.5	191.4	3.9	24.0	31.4
SMP 10	−13.12	0.16	377.2	1115.5	6.1	324.0	19.0	...	0.0	...
SMP 13	−12.88	0.09	353.8	1068.2	4.2	1.4	1.5	7.2	306.1	15.0	2.9	3.1	3.3
SMP 16	−13.22	0.14	293.7	843.2	26.6	...	9.3	196.4	318.5	628.7	...	42.4	44.9
SMP 18	−13.46	0.07	274.0	841.0	300.6	...	3.6
SMP 19	−12.88	0.18	442.7	1320.6	16.0	3.9	5.9	36.8	329.8	109.9	3.5	13.7	20.8
SMP 25	−12.39	0.12	268.3	800.0	3.8	1.1	1.3	7.2	314.6	22.7	4.5	1.1	2.1
SMP 27	−13.54	0.06	261.2	769.2	299.0	3.8	5.0
SMP 28	−13.57	0.32	310.4	925.4	17.3	6.7	9.3	53.0	369.0	466.4	7.6	13.5	17.8
SMP 30	−13.50	0.11	233.4	684.7	291.1	311.8	843.9	...	52.5	55.4
SMP 31	−12.92	0.54	34.9	100.0	3.4	1.0	1.2	24.5	441.2	78.1	3.6
SMP 34	−12.97	0.06	174.1	511.1	3.4	300.0	13.1	3.8	1.0	0.9
SMP 46	−13.53	0.18	396.6	1200.0	20.9	5.1	7.4	68.5	328.1	212.2	5.7	19.5	28.6
SMP 53	−12.67	0.13	401.4	1223.3	8.8	2.9	2.8	20.3	315.8	61.9	3.7	5.5	8.7
SMP 58	−12.54	0.11	228.2	666.7	2.7	1.6	0.7	2.4	312.0	8.2	4.5	0.2	0.6
SMP 59	−13.16	...	206.9	604.9	211 ^a	41.8 ^b	...
SMP 65	−13.44	0.22	211.5	717.8	339.7	...	4.9
SMP 71	−12.90	0.24	392.1	1182.5	14.5	2.7	5.3	29.9	344.4	88.9	3.8	8.1	13.2
SMP 78	−12.60	0.21	456.3	1377.0	9.6	2.6	3.4	17.4	337.3	52.0	3.6	3.1	6.5
SMP 79	−12.68	0.18	421.8	1260.7	9.3	2.6	3.4	8.6	328.4	30.5	4.1	2.6	5.1

Table 2—Continued

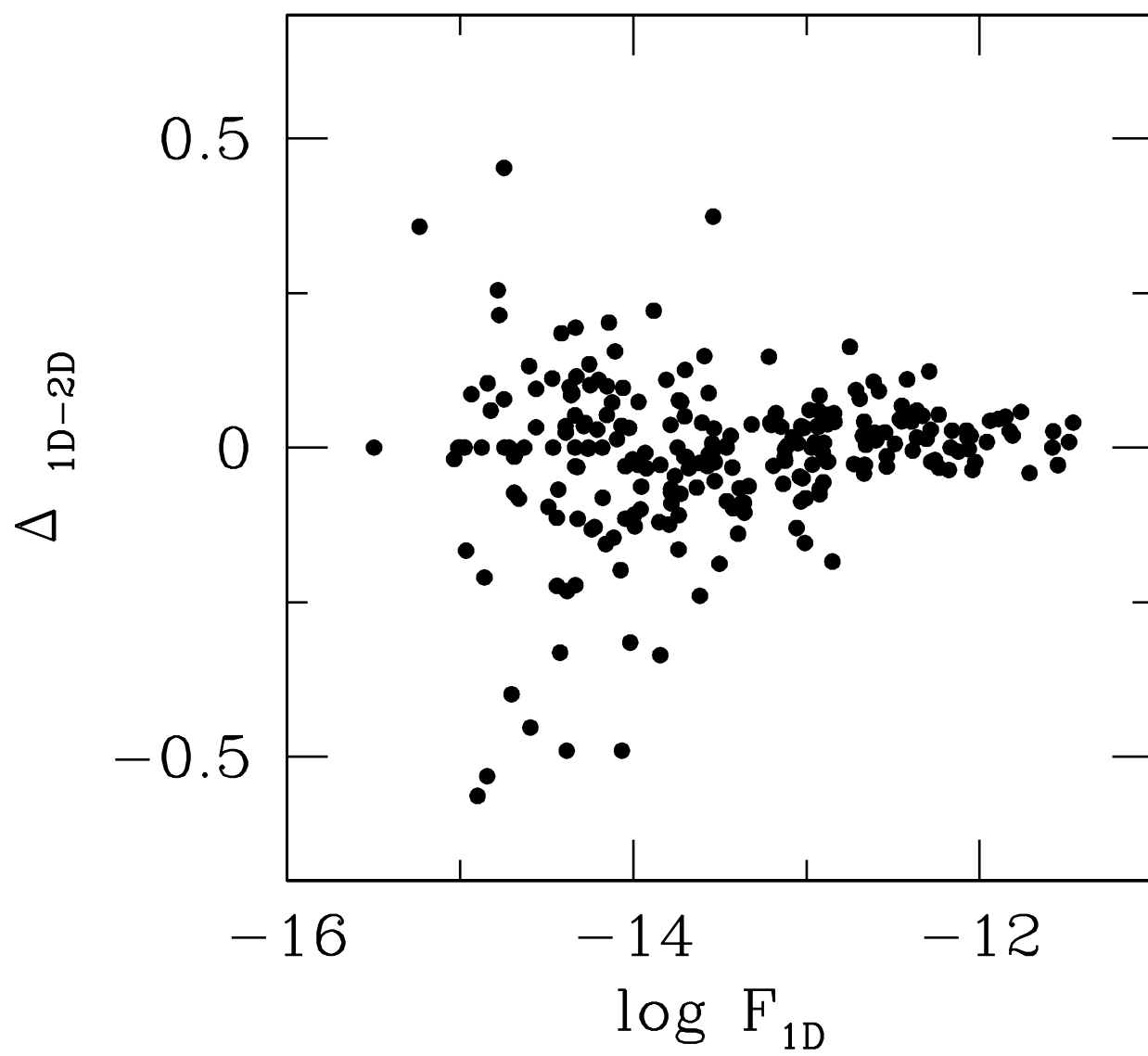
	$F(\text{H}\beta)$		[OIII]	[OIII]	[OI]	[SIII]	[OI]	[NII]	H α	[NII]	HeI	[SII]	[SII]
Nebula	(4861)	c	(4959)	(5007)	(6300)	6312	6363	(6548)	(6563)	6584	6678	(6716)	(6731)
(1)	(2)	(3)	(4)	(5)	(6)	(7)	(8)	(9)	(10)	(11)	(12)	(13)	(14)
SMP 80	−13.18	0.08	175.7	533.0	10.6	304.8	29.9	4.1	3.1	4.1
SMP 81	−12.66	0.24	434.6	1304.1	4.7	3.2	1.7	5.1	347.0	18.5	4.4	0.6	1.6
SMP 93	−13.05	...	134.4	403.1	36.3	...	13.2	...	427 ^a	51.4 ^b	...
SMP 94 ^c	−13.06	1.05	18.8	52.9	663.6
SMP 95	−13.46	0.11	335.3	1008.7	32.4	28.8	12.9	72.6	312.0	219.0	10.9	28.9	31.2
SMP 100	−12.88	0.02	391.7	1165.4	3.1	5.7	289.5	21.7	...	2.4	3.5
SMP 102	−13.21	^d	235.0	703.4	...	3.8	...	1.6	228.5	4.1	2.9

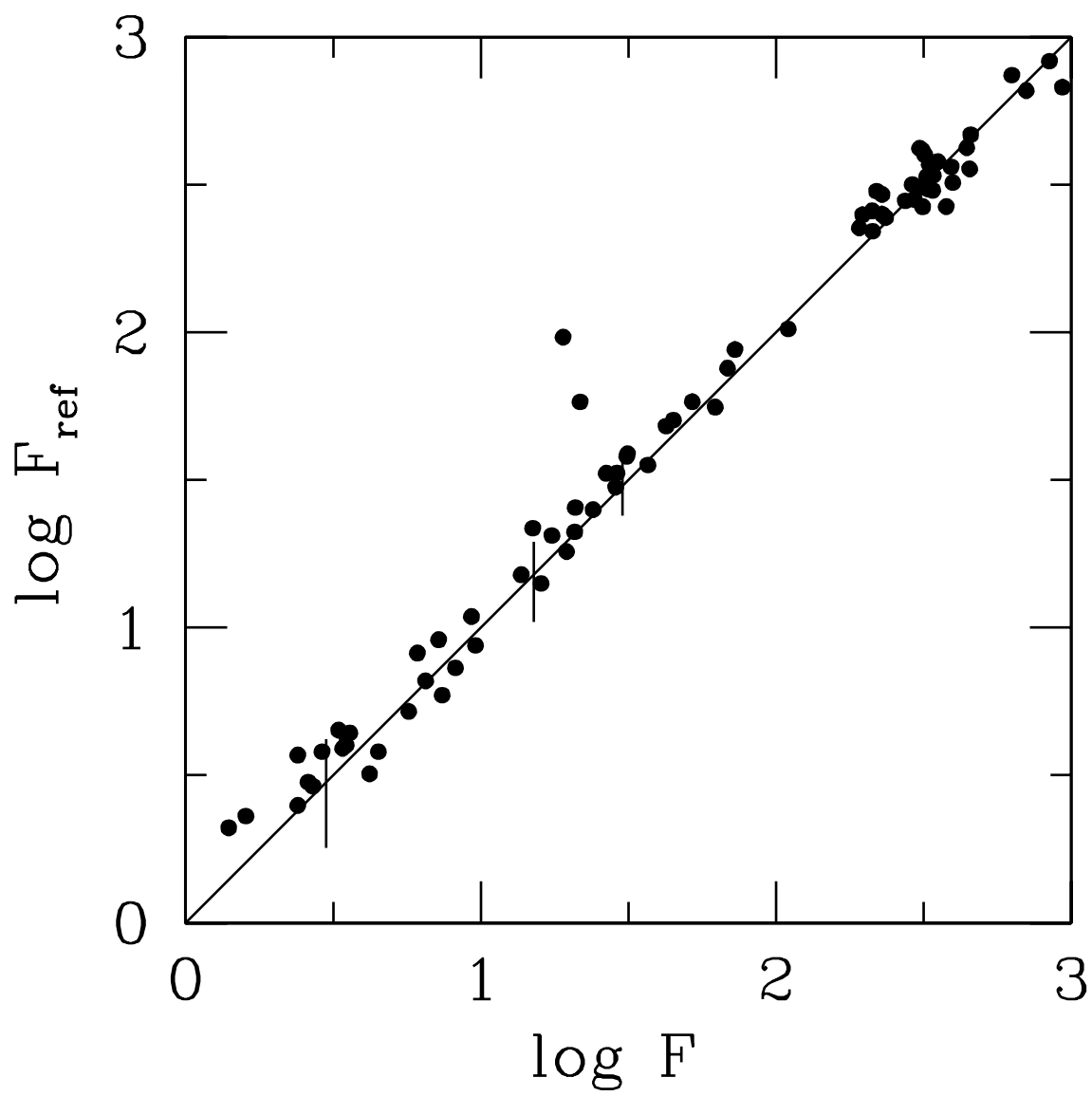
^aIntensity of the blend of H α and [NII] λ 6548, 6584.

^bIntensity of the blended doublet [SII] λ 6716,6731.

^cProbably not a PN.

^dNegative extinction.

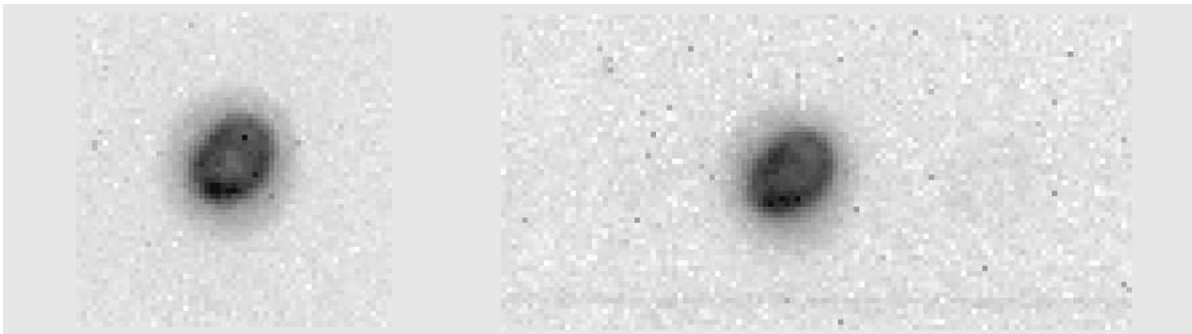




J 41



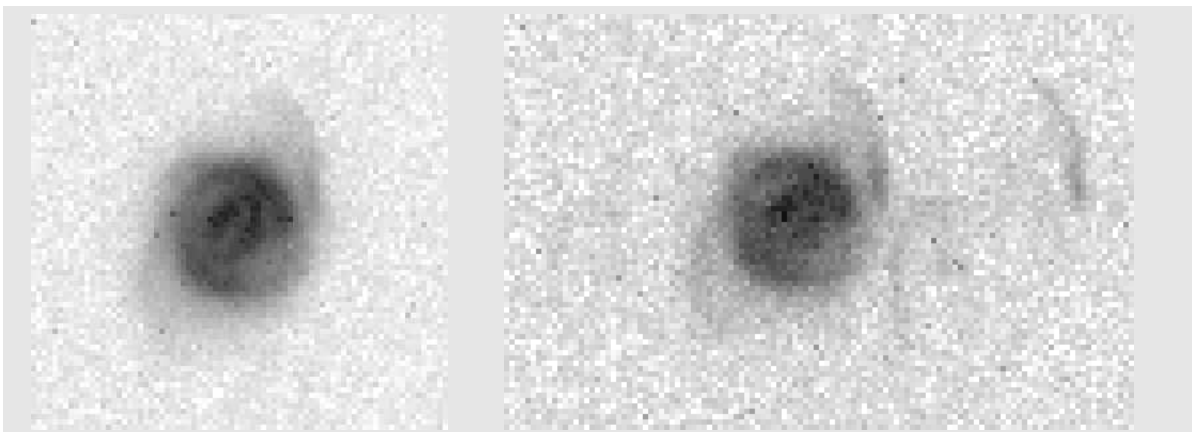
SMP 4



SMP 9



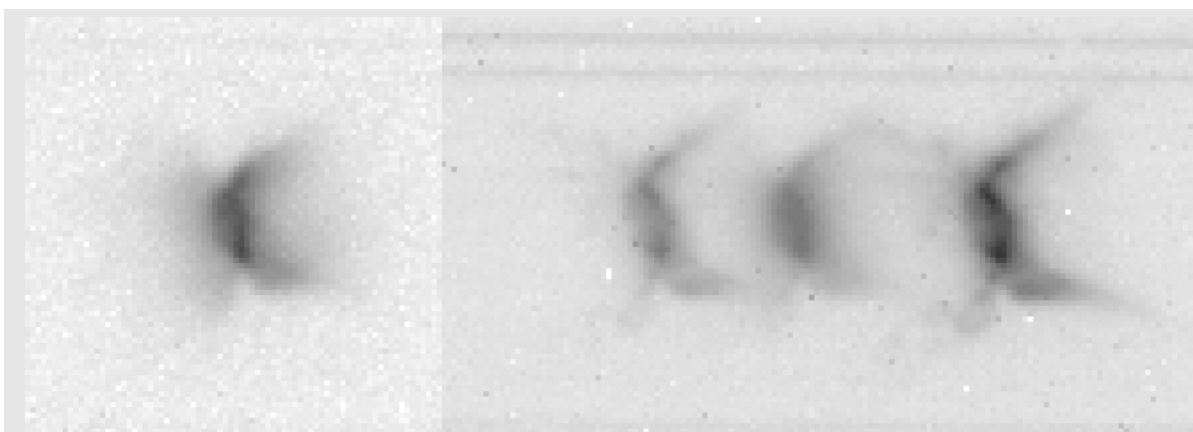
SMP 10



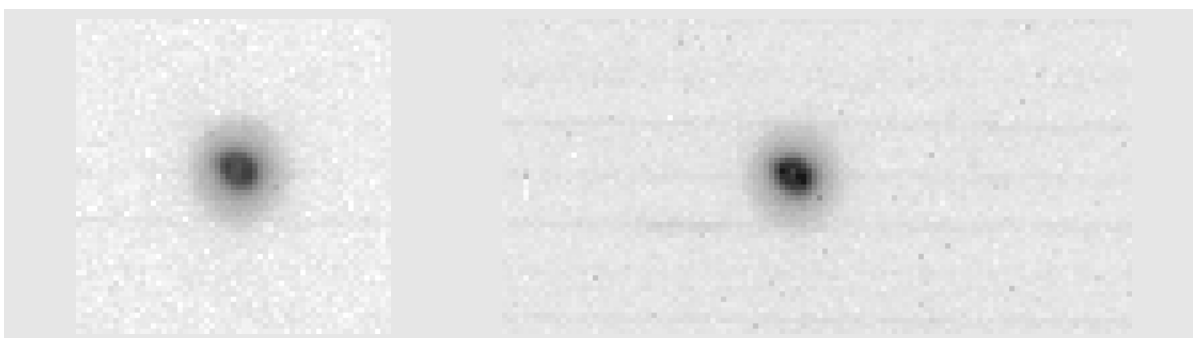
SMP 13



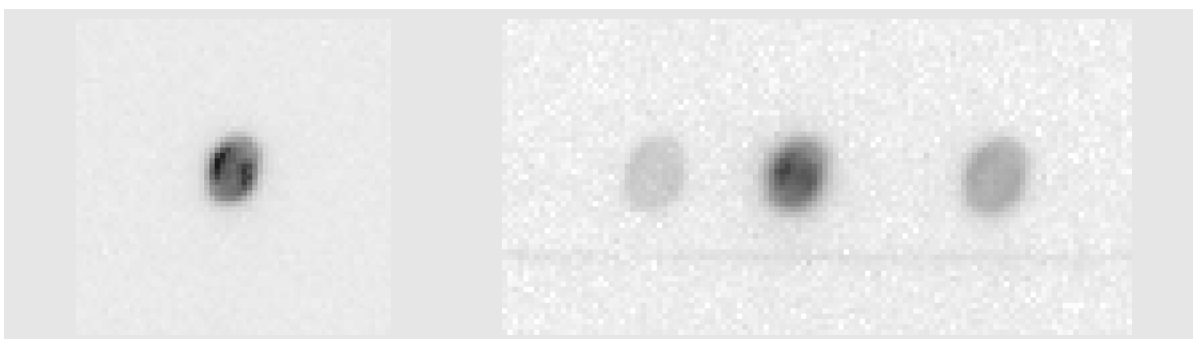
SMP 16



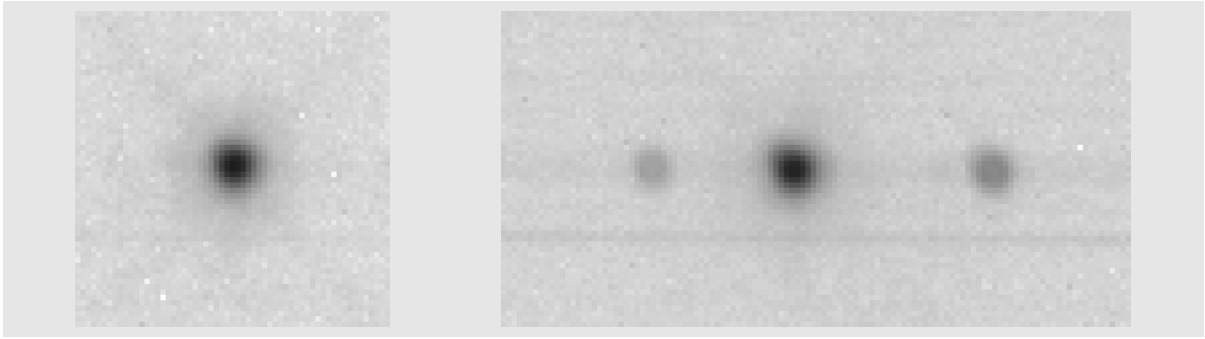
SMP 18



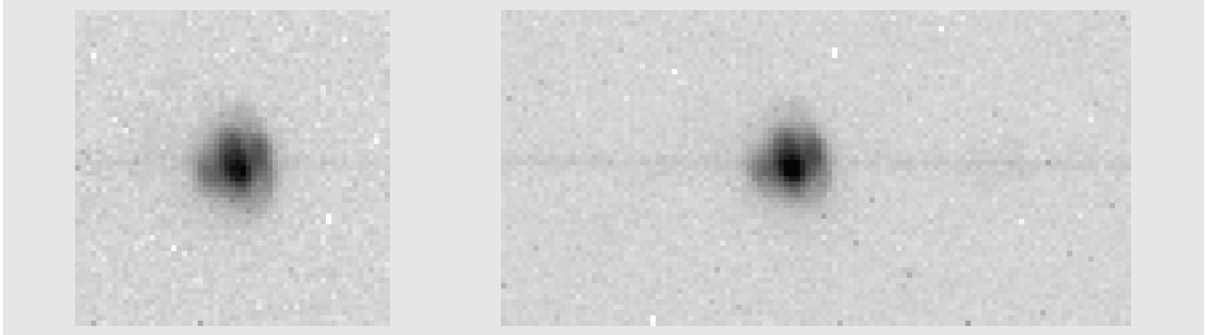
SMP 19



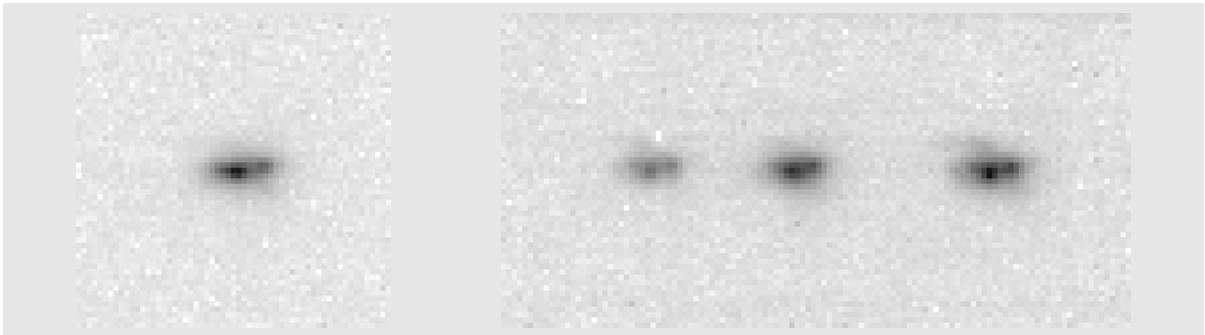
SMP 25



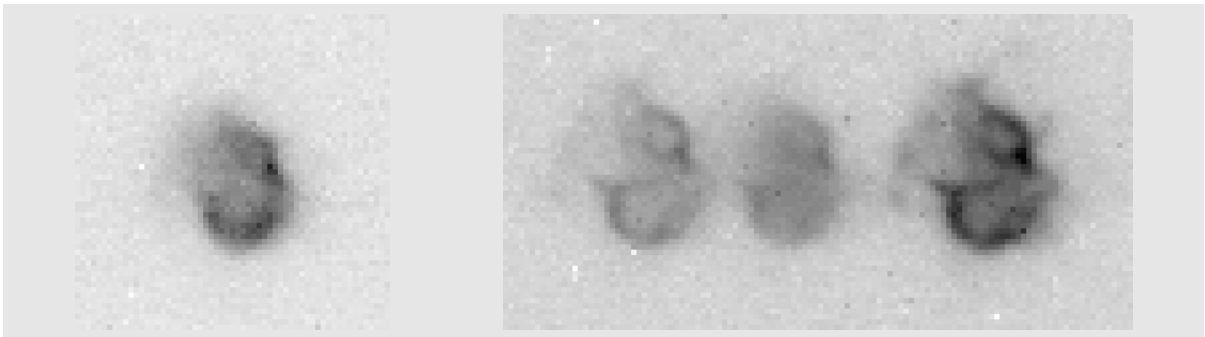
SMP 27



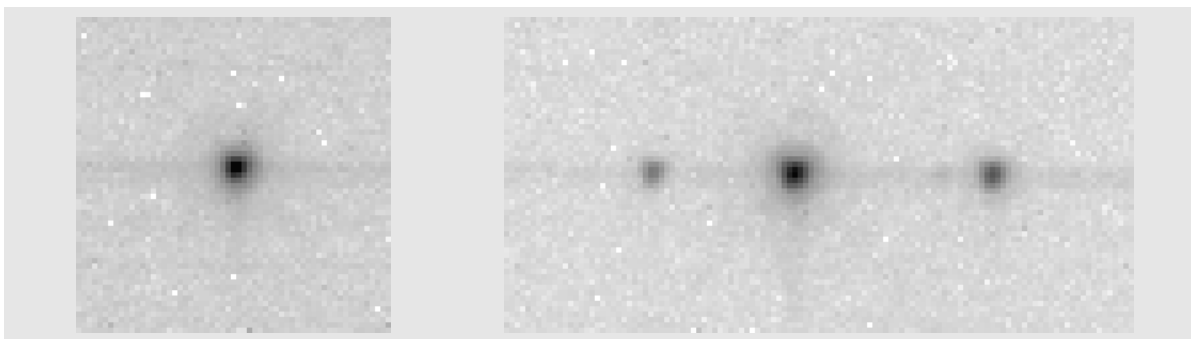
SMP 28



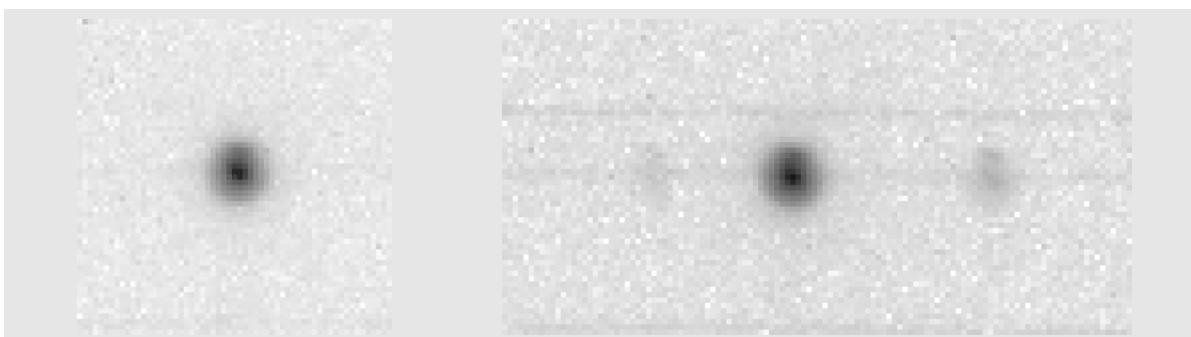
SMP 30



SMP 31



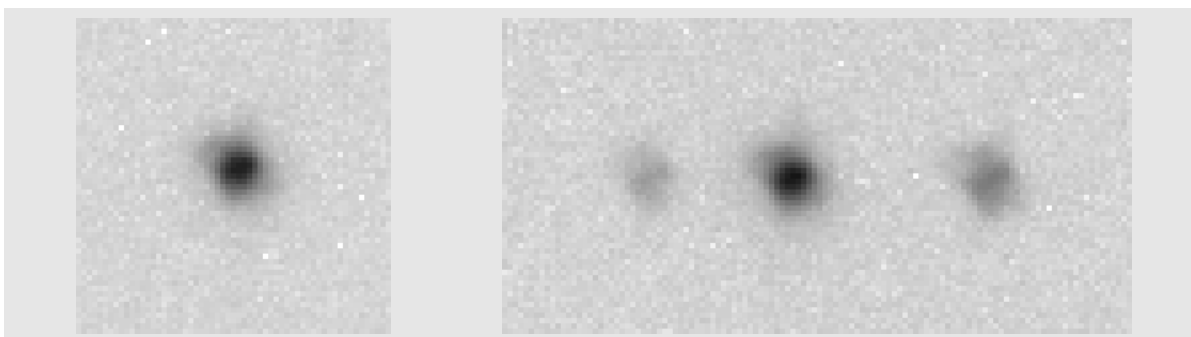
SMP 34



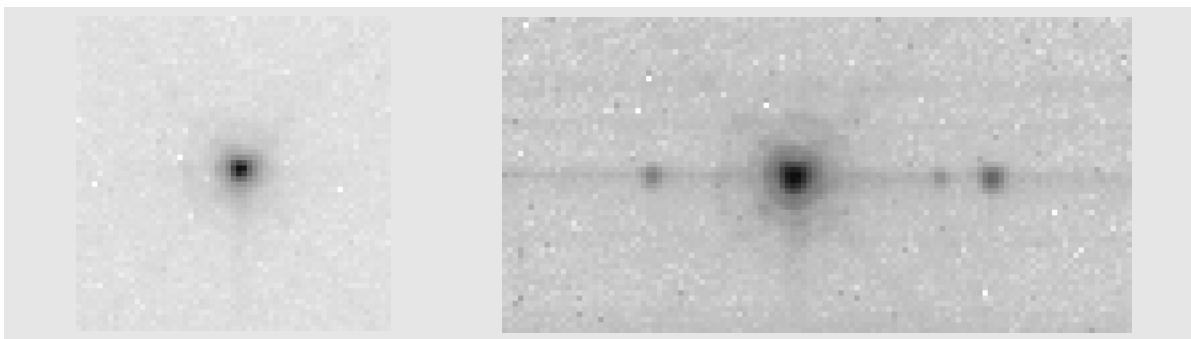
SMP 46



SMP 53



SMP 58



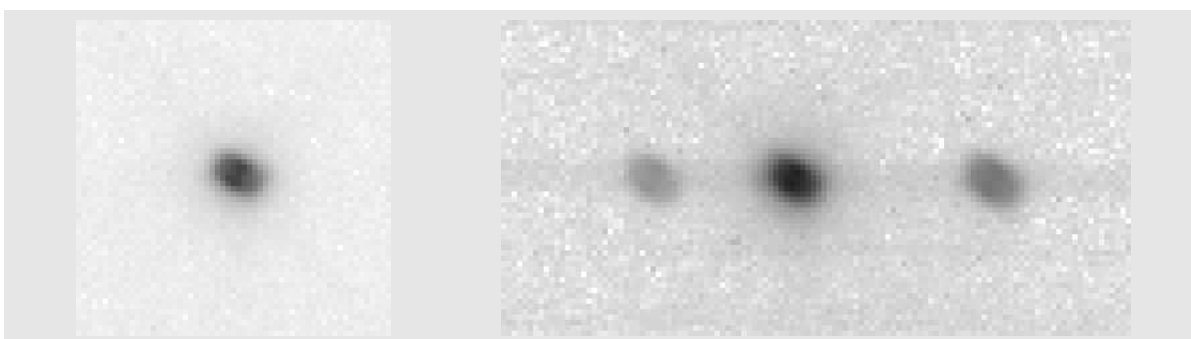
SMP 65



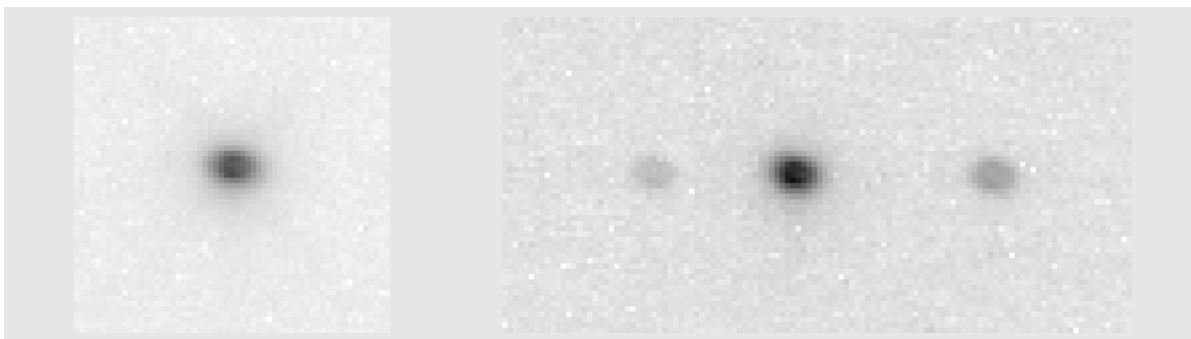
SMP 71



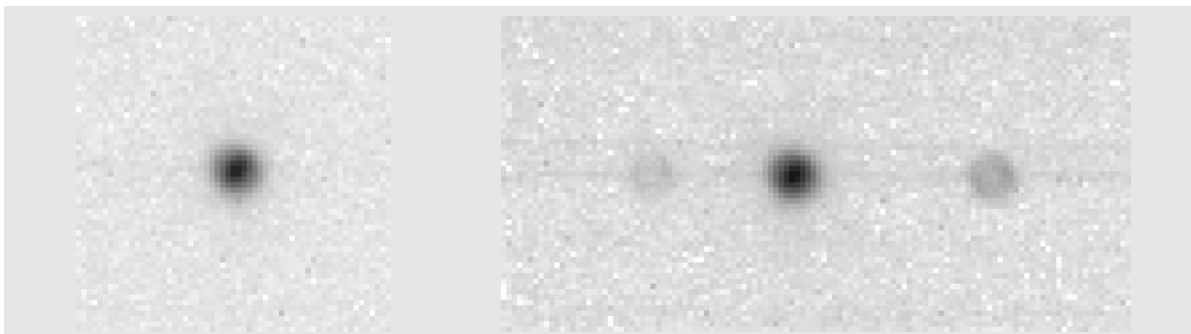
SMP 78



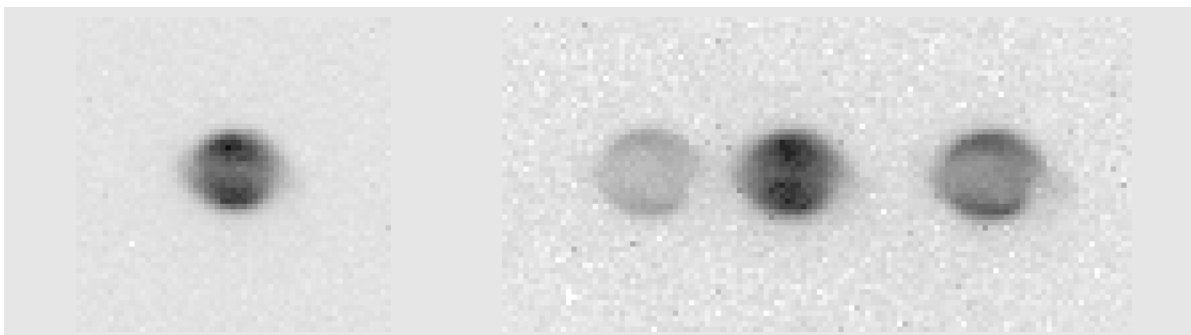
SMP 79



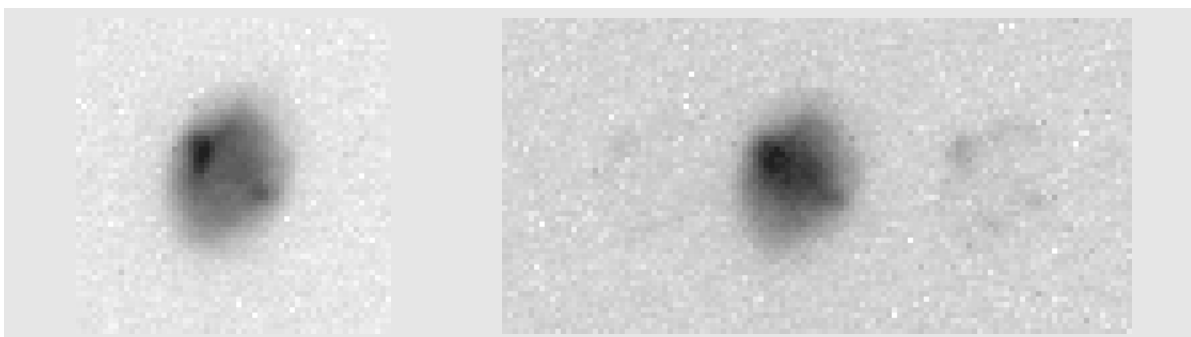
SMP 80



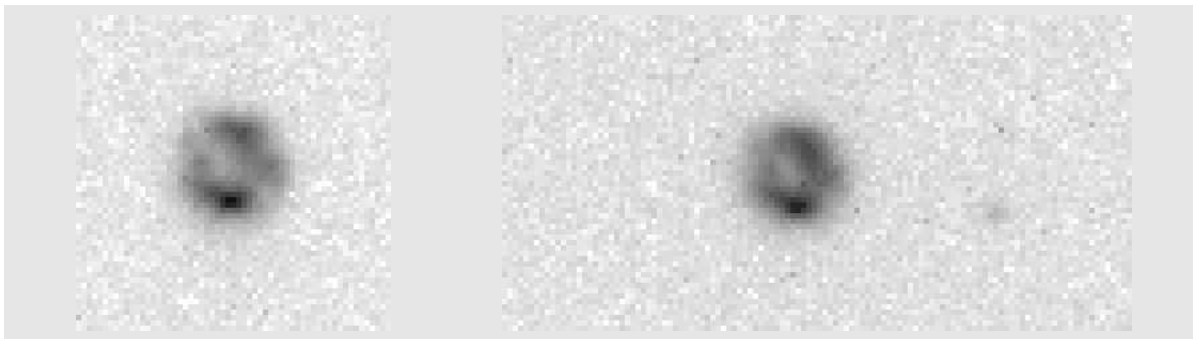
SMP 95



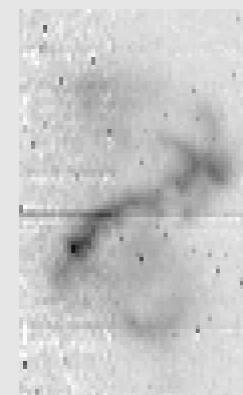
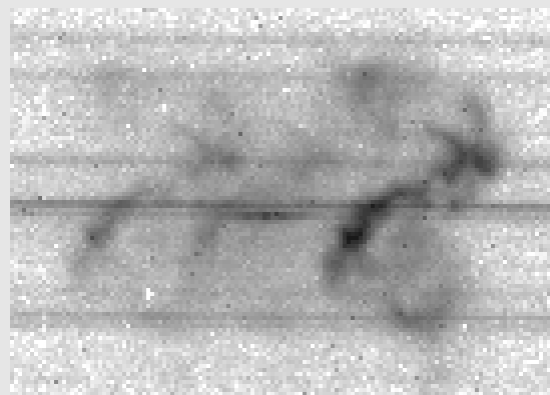
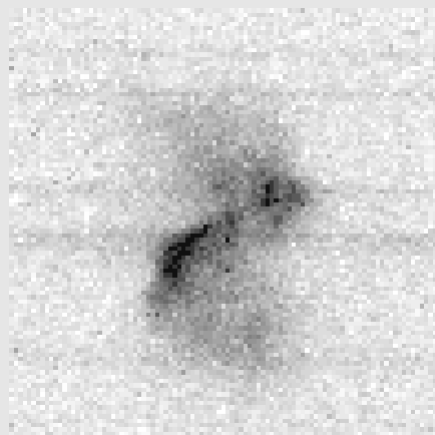
SMP 100



SMP 102



SMP 59



SMP 93

